3-12-2018

Humans Thrived in South Africa through the Toba Eruption about 74,000 Years Ago

Eugene I. Smith
University of Nevada, Las Vegas, gene.smith@unlv.edu

Zenobia Jacobs
University of Wollongong

Racheal Johnsen
University of Nevada, Las Vegas

Minghua Ren
University of Nevada, Las Vegas, minghua.ren@unlv.edu

Erich C. Fisher
Arizona State University
Follow this and additional works at: https://digitalscholarship.unlv.edu/geo_fac_articles

Part of the Archaeological Anthropology Commons, and the Geology Commons
See next page for additional authors

Repository Citation

Authors

Eugene I. Smith, Zenobia Jacobs, Racheal Johnsen, Minghua Ren, Erich C. Fisher, Simen Oestmo, Jayne Wilkins, Jacob A. Harris, Panagiotis Karkanas, Shelby Fitch, Amber Ciravolo, Deborah Keenan, Naomi Cleghorn, Christine S. Lane, Thalassa Matthews, and Curtis W. Marean

LETTER

Humans thrived in South Africa through the Toba eruption about 74,000 years ago

Eugene I. Smith[1], Zenobia Jacobs[2], Racheal Johnsen[1], Minghua Ren[1], Erich C. Fisher[3,4], Simen Oestmo[4], Jayne Wilkins[5], Jacob A. Harris[3], Panagiotis Karkanas[6], Shelby Fitch[1], Amber Ciravolo[1], Deborah Keenan[7], Naomi Cleghorn[4,8], Christine S. Lane[9], Thalassa Matthews[10] & Curtis W. Marean[3,4]

Approximately 74 thousand years ago (ka), the Toba caldera erupted in Sumatra. Since the magnitude of this eruption was first established, its effects on climate, environment and humans have been debated[1]. Here we describe the discovery of microscopic glass shards characteristic of the Youngest Toba Tuff—ashfall from the Toba eruption—in two archaeological sites on the south coast of South Africa, a region in which there is evidence for early human behavioural complexity. An independently derived dating model supports a date of approximately 74 ka for the sediments containing the Youngest Toba Tuff glass shards. By defining the input of shards at both sites, which are located nine kilometres apart, we are able to establish a close temporal correlation between them. Our high-resolution excavation and sampling technique enable exact comparisons between the input of Youngest Toba Tuff glass shards and the evidence for human occupation. Humans in this region thrived through the Toba event and the ensuing full glacial conditions, perhaps as a combined result of the uniquely rich resource base of the region and fully evolved modern human adaptation.

We use a date of approximately 74 ka as the time of eruption of the Youngest Toba Tuff (YTT), just before the onset of glacial marine isotope stage 4 (MIS4)[2,3]. Early modern humans evolved in Africa before 100 ka and their main dispersal out of Africa began at about 70 ka[4]. To examine the potential effect of the Toba eruption on early modern humans[5] requires the identification of the YTT signature directly intermixed with the behavioural traces of modern humans in Africa, which we have achieved in the sites discussed here.

Tephra—fragmented material from an explosive volcanic eruption—ranges in size from macroscopic layers to microscopic glass shards of 'cryptotephra' that are deposited in sediments[6]. We discovered YTT glass shards in archaeological sediments at the sites of Vleesbaai area B (VBB) and Pinnacle Point Site 5-6 (PP5-6) on the south coast of South Africa (Fig. 1 and Extended Data Fig. 1). To our knowledge, this is the first successful identification and analysis of shards at such a great distance (approximately 9,000 km) from a source volcano; the identification of shards at both sites, located 8.7 km apart, provides an unusually high-precision temporal link between an open-air site and a rock shelter that were probably used by the same group of people.
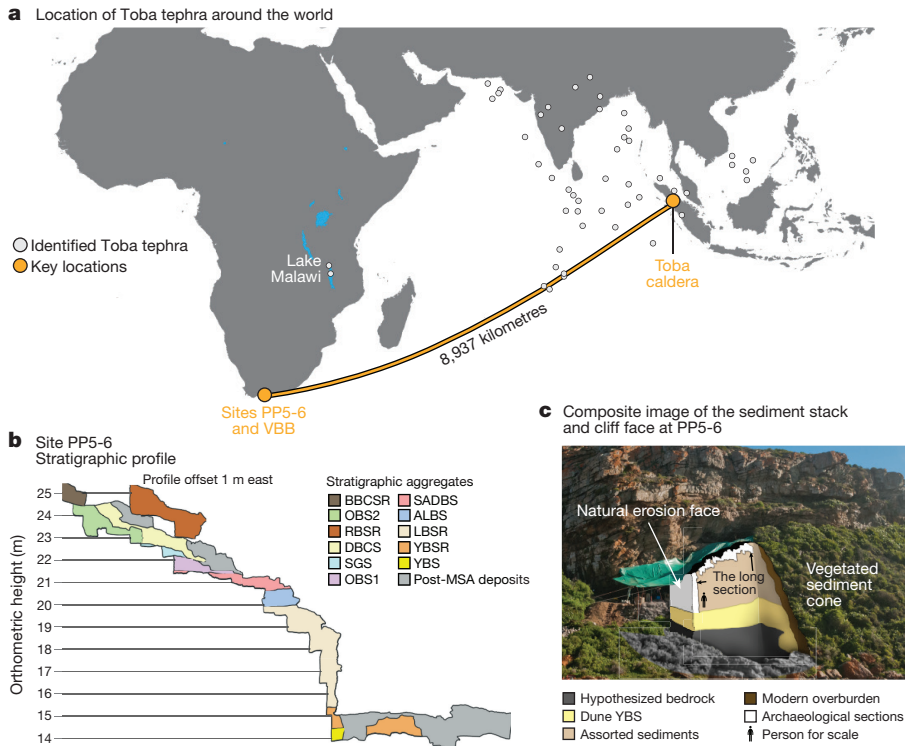
The published dates for the PP5-6 sequence range from approximately 90 to 50 ka, and are based on single-grain optically stimulated luminescence (OSL) dating[7]. We present an updated age model (Fig. 2) for PP5-6, constructed from 90 OSL-dated sediment samples analysed with Bayesian statistics, and calculated on the OxCal platform (https://c14.arch.ox.ac.uk/oxcal.html, see Methods and Supplementary

Information), for comparison to the distribution of YTT glass shards (see Methods). The rapid deposition and repeated occupation of the site by humans has created an approximately 15-vertical-metre, high-resolution record of human occupation across the timespan of the Toba eruption. The sediments at this site are grouped into large sedimentary units called 'aggregates'; thinner layers within these aggregates are referred to as 'sub-aggregates'[7]. The aggregates of interest here, from bottom to top, include 'light brown sand and roofspall' (LBSR), which is dated to about 90–74 ka, 'aeolian light brown sand' (ALBS) and 'shelly ashy brown sand' (SADBS), which together date to around 74–71 ka[7] (Fig. 2). We used total stations (see Methods) to measure the 3D location of over 400,000 archaeological finds to millimetre accuracy[8], which enables precise investigation of the relationship of the shards to the archaeological evidence for changes in the intensity of human occupation. We collected continuous sediment samples (2–3 g per sample) across these aggregates to search for shards (Fig. 2, Extended Data Figs 2–4 and Supplementary Videos 1–4).

At Vleesbaai, Later and Middle Stone Age occupations occur in stacked ancient dunes and palaeosols[9]. Excavations at VBB began in 2015, and have revealed lithic and faunal finds sealed below a post-depositional cemented layer. We excavated an area of 14 m² and recovered around 900 artefacts, which were plotted by total station and which came from a single lens that is limited to about a 10–15 cm vertical spread (Fig. 3). OSL and sediment samples were collected from an adjacent geological trench, located 6.8 m away from the archaeological excavation (Fig. 3). Two OSL samples from the artefact-bearing sediment, the aggregate 'dark yellowish-brown clayey sand' (DYBCS), give estimates dating to 73.4 ± 5.2 and 73.9 ± 4.2 ka. Two samples from the overlying 'light yellowish brown sand 2' (LYBS2) aggregate gave dates of 72.5 ± 4.3 and 71.4 ± 4.5 ka. The underlying 'strong brown clayey sand' (SBCS) aggregate was dated to 74.7 ± 5.8 ka, and the lowest unit—the 'very pale brown sand and concretions' (VPBSC) aggregate—was dated to 98.7 ± 7.6 ka. To determine whether cryptotephra shards were present, we collected continuous sediment samples at 1-cm intervals from a vertical 1.5-m section of the geological trench, across the stratigraphic contacts between DYBCS, SBCS and underlying VPBSC.

The identification of the source and age of cryptotephra is a tool used to define isochrons for correlation of sediments across sites and regions[6]. Samples were processed using cryptotephra separation techniques[6,10] modified for 'extremely low abundance' cryptotephra (Supplementary Information). Major elements were analysed by electron microprobe, and trace elements were analysed by laser-ablation inductively coupled plasma mass spectrometry (LA-ICP-MS)

Figure 1 | VBB and PP5-6 and its relationship to other YTT study sites. a, Location of VBB and PP5-6 relative to the Toba caldera and other locations at which YTT ash has been found. **b**, Schematic profile of the stratigraphic sequence at PP5-6 that shows the major depositional changes. **c**, Composite view of PP5-6 that shows an interpretation of how

the sediment stack developed in front of the cliff face, and its relation to the 'long section' excavation area. BBCSR, brown and black compact sand and roofspall; DBCS, dark brown compact sand; OBS, orange brown sand; RBSR, reddish brown sand and roofspall; SGS, shelly grey sand; YBS, yellowish brown sand; YBSR, yellowish brown sand and roofspall.
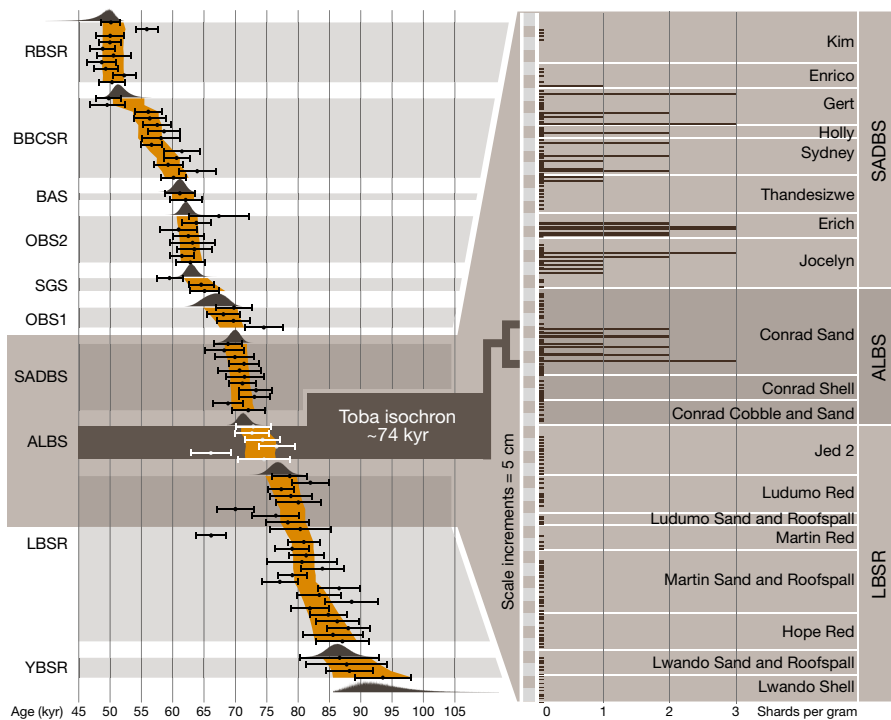
Figure 2 | The location of the YTT isochron at PP5-6. Left, current PP5-6 age model developed using OxCal v.4.2 (https://c14.arch.ox.ac. uk/oxcal.html) from OSL ages. Individual OSL ages are shown with their standard errors. The modelled boundaries between the stratigraphic aggregates are represented using the 95.4% confidence interval, whereas the continuous age model is represented at the 68% confidence interval. Right, details at the LBSR–ALBS and the ALBS–SADBS contacts, including

the distribution of YTT glass shards throughout this sequence for all shard sample transects. The shard counts are compiled by calculating the relative height of each sample above the lowermost stratigraphic sub-aggregate contact along each transect line, to compensate for lateral topographic variations across the sections. The YTT isochron is identified in the ALBS Conrad Sand. kyr, thousand years; BAS, black ashy sand.
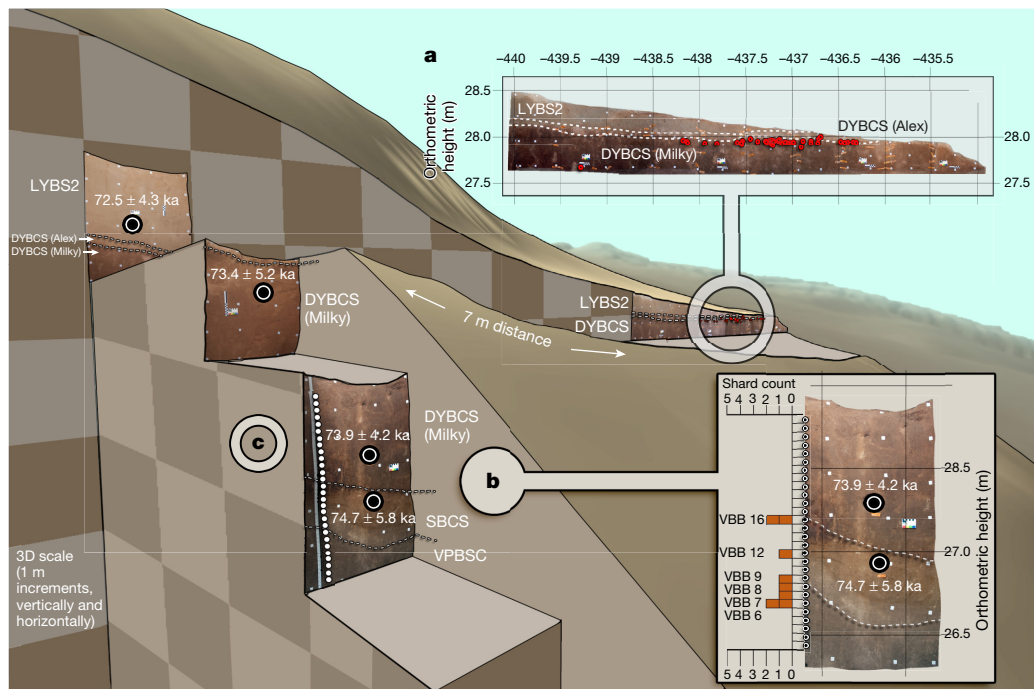
Figure 3 | The shard distribution, OSL dates and artefact plots as a composite digital cutaway at VBB. a, VBB site stratigraphy and 3D plotted artefacts on a digitally rectified stratigraphic photograph. **b**, Shard distribution on a digitally rectified stratigraphic photograph. **c**, Composite digital cutaway of VBB dune deposits showing stacked stratigraphic profiles in the north–south geological trench, and the east–west stratigraphic profile in the nearby archaeological excavations. OSL dating samples are indicated with black-and-white dots.

or secondary ion mass spectrometry (SIMS) (see Methods). We searched the databases of the 'Volcano Global Risk Identification and Analysis Project' (VOGRIPA; http://www.bgs.ac.uk/vogripa/), the Smithsonian Institution's 'Global Volcanism Program' (https://volcano.si.edu/) and the Petrological Database (http://www.earthchem.org/petdb) for moderate-to-large rhyolitic eruptions that occurred between 90 and 40 ka, and used these as the bases of comparison for all available compositional data. Only the YTT produced tephra that matched the major- and rare-earth-element chemistry of cryptotephra at VBB and PP5-6, and was of the proper age to contribute tephra to these sites (Fig. 4, Extended Data Figs 5, 6, Extended Data Tables 1, 2 and Supplementary Tables 1–5).

The major-element chemistry of cryptotephra from VBB is nearly identical to that of distal YTT previously described from India[11] and Lake Malawi[12] and to trace-element abundances in distal YTT glass[11] and rhyolite from the Toba caldera[13]. Cryptotephra from PP5-6 are a close match for YTT, but are slightly offset (see Supplementary Discussion). The shards from PP5-6 are in sediments below the drip line at PP5-6. This zone is a complex depositional environment[7], and these shards may therefore have been subjected to chemical alteration that has resulted in the chemical differences between PP5-6 crypto-tephra and typical distal YTT cryptotephra.

We built a Bayesian model to formally assign the probability that individual shards belong to a known eruption (see Methods). When applied to shards from VBB and PP5-6, the model shows that, for each shard analysis, there is a >96% probability that they correlate with YTT (Extended Data Tables 3, 4, Methods and Supplementary Tables 8–10). Despite the slight chemical offset of the PP5-6 shards, the chemical plots and Bayesian model show that these shards more closely match YTT than any other known eruption. The fact that shards at VBB are a near-perfect match to YTT cryptotephra, and that OSL dates for the sediments at both sites correspond to the age of the Toba eruption, leads us to conclude that Toba is the source volcano for both sets of shards. We recognize that the chemistry of the shards at PP5-6 is not a perfect match, probably as a result of post-depositional alteration. To our knowledge, these shards are

the farthest-travelling shards from any volcano that have yet been discovered.

We extracted and counted shards from the sediment samples to create a shard profile. The cryptotephra at PP5-6 display a vertical shard profile with a few sharp distinct peaks that are concentrated in ALBS sediments above the LBSR, with a fluctuating but generally diminishing shard content as one moves up the stratigraphy (Fig. 2). This pattern is typical of the near-instantaneous deposition of material after a volcanic eruption[6]. The first appearance and highest concentration of shards occurs near the top of an aeolian sand unit, the sub-aggregate 'Conrad Sand'. This first peak is overlain by an approximately 10-cm-thick layer of aeolian sand that is free of shards; this layer is sealed by a series of successive intact hearth features in the lower portion of 'Jocelyn' sub-aggregate that are also devoid of shards (Fig. 2). We place the YTT isochron at the position of Conrad Sand (Fig. 2 and Extended Data Fig. 4).

The transition from roofspall-dominated (LBSR) to aeolian-dominated (ALBS) sediments (Extended Data Fig. 4) indicates a major environmental change that reflects the onset of MIS4 and retreat of the sea[7]. The ALBS aeolian unit has within it one dense human occupation layer ('Conrad Shell') and several thin, less-dense human occupation lenses. The first tephra peak is located just above the Conrad Shell layer, and is interstratified with aeolian sand and evidence of human occupation. Our Bayesian age model dates the transition between LBSR and ALBS to 79.5–74.1 ka (95.4% probability for all dates). The YTT isochron in the Conrad Sand has two measured OSL dates of 72.6 ± 5.6 and 72.8 ± 5.8 ka, with Bayesian-modelled time intervals of 75.4–70.9 ka, both of which are statistically consistent with the approximately 74 ka estimate for YTT[2,3].

At VBB, the first occurrence of the shards is at the top of VPBCS, near where this aggregate contacts SBCS. A second occurrence in the shard profile occurs at the contact between SBCS and DYBCS (Fig. 3). No shards were recovered from sediments above this contact or below the top of VPBCS (Fig. 3). The cryptotephra-bearing sediments at VBB have OSL dates of between 73.9 ± 4.2 and 74.7 ± 5.8 ka and thus are also statistically consistent with the age of YTT. The artefacts were
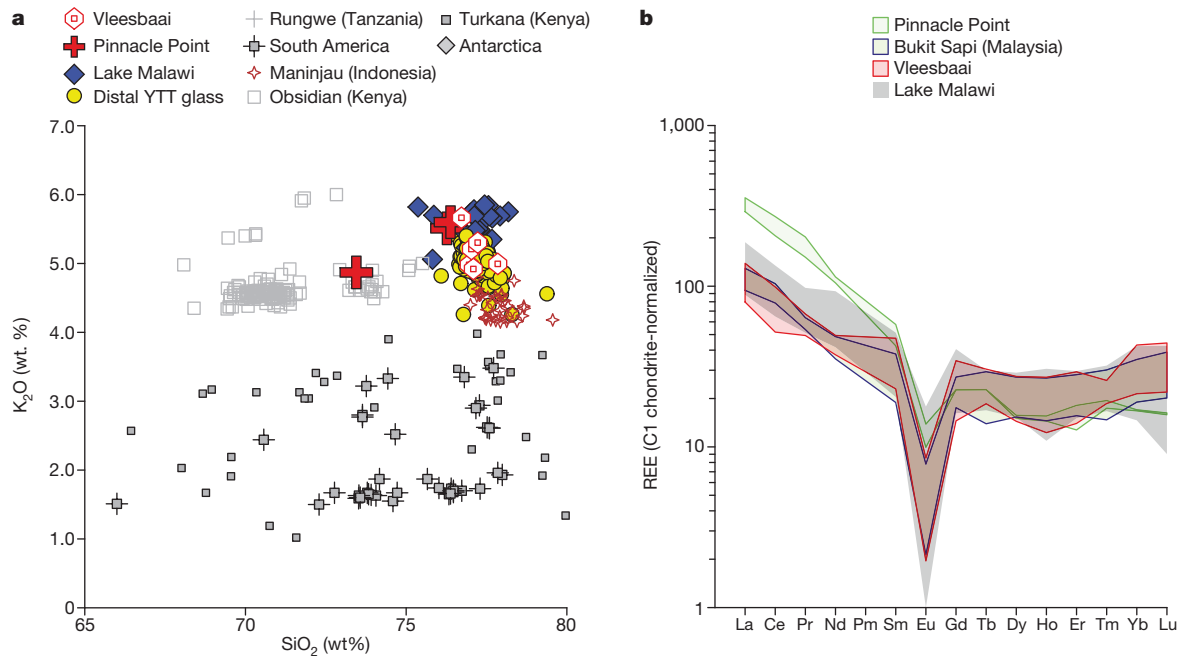
Figure 4 | Geochemical comparisons between extremely low abundance cryptotephra at VBB and PP5-6, and distal and proximal YTT.
a, **b**, K_2O versus SiO_2 (weight per cent, wt%) (**a**) and rare-earth elements (REE) normalized to chondrite (**b**) comparing VBB and PP5-6 shards to YTT glass. Gd and Tb were not analysed by SIMS. In **a**, tephra from other volcanoes in Indonesia (Maninjau), Africa (Rungwe and Turkana), Antarctica and South America (see Supplementary Information) are also plotted. In **a**, samples from Rungwe and Antarctica have SiO_2 values of less than 65 wt% and are not shown on the plots.

recovered from the top of DYBCS, about 1.5 m above the highest shard in the vertical profile. The OSL dates of 73.9 ± 4.2 and 73.4 ± 5.2 ka for the bottom and top of DYBCS, respectively, are consistent with the deposition of the VBB artefacts at around 74 ka, at—or shortly after—the deposition of YTT cryptotephra.

Finding YTT in both the PP5-6 and VBB sedimentary sequences illustrates the transformative potential in being able to temporally link multiple sites, including open-air focused activity sites and home-base sites such as rock shelters or caves. The Toba event has previously been located in both the Greenland and Antarctic ice cores, where synchronous volcanic markers have been identified within Greenland interstadial 20 (Antarctic isotope maxima 19 and 20)[14], and thus form an isochron from archaeological sites in South Africa to Greenland, around 13,000 km apart.

At PP5-6, the LBSR-to-ALBS transition and YTT isochron accompanies changes from low-intensity human occupation (in LBSR) to high-intensity occupation coupled with intense anthropogenic burning (in SADBS)[7]. The frequency of plotted finds (for example, bone, stone artefacts and so on) and lack of gaps in the stratigraphy shows that the occupation of PP5-6 after YTT was intense and continuous (Fig. 5 and Supplementary Videos 1–4). A 3D density analysis (see Methods) demonstrates that the amount of plotted finds remained continuous across the YTT event and increased in SADBS. The SADBS aggregate also contains a technological change, marked by the consistent use of heat-treated silcrete to produce stone tools and a commitment to advanced microlithic technology[15]. Not only did modern human populations on the south coast of South Africa survive the YTT event, but also the intensity of site use increased after this event, and a series of technological innovations appeared shortly after YTT and persisted for thousands of years[15].

The southern African sub-region[16] and south coast[17,18] are candidate regions for housing the origin population of modern humans, and represent potential refuge zones during harsh climate cycles. It has previously been suggested that the Toba eruption caused a volcanic winter that devastated human populations[5,19], and a previously

The PP5-6 sediment stack profile
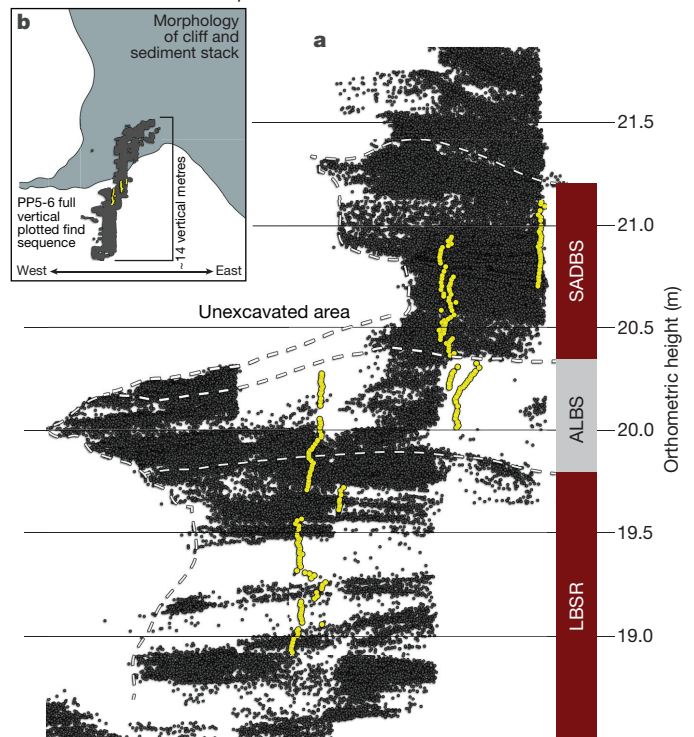
Figure 5 | The density of plotted finds across the upper LBSR, ALBS, and SADBS at PP5-6. This figure shows the distribution of plotted archaeological and faunal materials at PP5-6. Each dark grey point represents a single artefact, bone or shell. The yellow dots are sediment samples collected for analysis. The white dashes indicate the extent of the stratigraphic aggregate indicated as LBSR, ALBS or SADBS on the right. See Supplementary Videos 1–4 for 3D renderings of these data.

published climate model[20] has suggested that the YTT eruption had a decades-long negative effect on world terrestrial ecosystems. Our excavations at PP5-6 may, therefore, have intercepted a population in a coastal refuge during the hypothetical volcanic winter. Our results raise the question of whether the modern human population on the south coast of South Africa was the sole surviving population through a decade or more of volcanic winter, or whether populations elsewhere in Africa thrived through the YTT event and the ensuing MIS4 glacial phase. This question can now be tackled by applying the same suite of field and laboratory procedures[8,21,22] used here to other archaeological sites in Africa.

Online Content Methods, along with any additional Extended Data display items and Source Data, are available in the online version of the paper; references unique to these sections appear only in the online paper.

1. Williams, M. The ~73 ka Toba super-eruption and its impact: history of a debate. *Quat. Int.* **258**, 19–29 (2012).
2. Storey, M., Roberts, R. G. & Saidin, M. Astronomically calibrated $^{40}Ar/^{39}Ar$ age for the Toba supereruption and global synchronization of late Quaternary records. *Proc. Natl Acad. Sci. USA* **109**, 18684–18688 (2012).
3. Mark, D. F. *et al.* A high-precision $^{40}Ar/^{39}Ar$ age for the Young Toba Tuff and dating of ultra-distal tephra: forcing of Quaternary climate and implications for hominin occupation of India. *Quat. Geochronol.* **21**, 90–103 (2014).
4. Marean, C. W. An evolutionary anthropological perspective on modern human origins. *Annu. Rev. Anthropol.* **44**, 533–556 (2015).
5. Rampino, M. R. & Ambrose, S. H. in *Volcanic Hazards and Disasters in Human Antiquity* (eds McCoy, F. W. & Heiken, G.) 71–82 (Geological Society of America, 2000).
6. Lane, C. S., Cullen, V. L., White, D., Bramham-Law, C. W. F. & Smith, V. C. Cryptotephra as a dating and correlation tool in archaeology. *J. Archaeol. Sci.* **42**, 42–50 (2014).
7. Karkanas, P., Brown, K. S., Fisher, E. C., Jacobs, Z. & Marean, C. W. Interpreting human behavior from depositional rates and combustion features through the study of sedimentary microfacies at site Pinnacle Point 5-6, South Africa. *J. Hum. Evol.* **85**, 1–21 (2015).
8. Oestmo, S. & Marean, C. W. in *Field Archaeology from Around the World* (eds Carver, M. B. *et al.*) 5955–5959 (Springer, 2015).
9. Oestmo, S., Schoville, B. J., Wilkins, J. & Marean, C. W. A Middle Stone Age paleoscape near the Pinnacle Point caves, Vleesbaai, South Africa. *Quat. Int.* **350**, 147–168 (2014).
10. Blockley, S. P. E. *et al.* A new and less destructive laboratory procedure for the physical separation of distal glass tephra shards from sediments. *Quat. Sci. Rev.* **24**, 1952–1960 (2005).
11. Smith, V. C. *et al.* Geochemical fingerprinting of the widespread Toba tephra using biotite compositions. *Quat. Int.* **246**, 97–104 (2011).
12. Lane, C. S., Chorn, B. T. & Johnson, T. C. Ash from the Toba supereruption in Lake Malawi shows no volcanic winter in East Africa at 75 ka. *Proc. Natl Acad. Sci. USA* **110**, 8025–8029 (2013).
13. Westgate, J. A. *et al.* Tephrochronology of the Toba Tuffs: four primary glass populations define the 75-ka Youngest Toba Tuff, northern Sumatra, Indonesia. *J. Quat. Sci.* **28**, 772–776 (2013).
14. Svensson, A. *et al.* Direct linking of Greenland and Antarctic ice cores at the Toba eruption (74 ka BP). *Clim. Past* **9**, 749–766 (2013).
15. Brown, K. S. *et al.* An early and enduring advanced technology originating 71,000 years ago in South Africa. *Nature* **491**, 590–593 (2012).
16. Henn, B. M. *et al.* Hunter-gatherer genomic diversity suggests a southern African origin for modern humans. *Proc. Natl Acad. Sci. USA* **108**, 5154–5162 (2011).
17. Marean, C. W. Pinnacle Point Cave 13B (Western Cape Province, South Africa) in context: the Cape Floral kingdom, shellfish, and modern human origins. *J. Hum. Evol.* **59**, 425–443 (2010).
18. Marean, C. W. *et al.* in *Fynbos: Ecology, Evolution, and Conservation of a Megadiverse Region* (eds Allsopp, N. *et al.*) 164–199 (Oxford Univ. Press, 2014).
19. Ambrose, S. H. Late Pleistocene human population bottlenecks, volcanic winter, and differentiation of modern humans. *J. Hum. Evol.* **34**, 623–651 (1998).
20. Robock, A. *et al.* Did the Toba volcanic eruption of ~74 ka B.P. produce widespread glaciation? *J. Geophys. Res. Atmos.* **114**, D10107 (2009).
21. Fisher, E. C. *et al.* Technical considerations and methodology for creating high-resolution, color-corrected, and georectified photomosaics of stratigraphic sections at archaeological sites. *J. Archaeol. Sci.* **57**, 380–394 (2015).
22. Bernatchez, J. A. & Marean, C. W. Total station archaeology and the use of digital photography. *SAA Archaeol. Rec.* **11**, 16–21 (2011).

Author Contributions C.W.M. conceived and coordinated the study, and directed the fieldwork at PP5-6; S.O. and J.W. directed fieldwork at the Vleesbaai site; C.S.L. advised and assisted with cryptotephra methods and results; E.C.F. conducted the geographic information systems analysis, shard distribution analysis and co-directed the excavations; E.I.S., A.C., S.O., D.K. and J.W. collected samples for the cryptotephra study; E.I.S., R.J. and S.F. processed samples, identified sources and constructed the profile; J.A.H. conducted the Bayesian analysis of the geochemistry; M.R. analysed shards by electron probe microanalysis; N.C. helped to direct the excavations and collected many of the samples; J.A.H. provided the statistical model; P.K. studied the sedimentology and geology of the site and first discovered the shards; T.M. is an excavation permit co-holder and contributes to the palaeoenvironmental studies; and Z.J. conducted the OSL dating and Bayesian modelling of OSL ages. All authors contributed to the writing of the paper.

Author Information Reprints and permissions information is available at www.nature.com/reprints. The authors declare no competing interests. Readers are welcome to comment on the online version of the paper. Publisher's note: Springer Nature remains neutral with regard to jurisdictional claims in published maps and institutional affiliations. Correspondence and requests for materials should be addressed to E.I.S. (gene.smith@unlv.edu) for tephra study, and C.W.M. (curtis.marean@asu.edu) for archaeology.

Reviewer Information *Nature* thanks S. Blockley, R. Grun and the other anonymous reviewer(s) for their contribution to the peer review of this work.

METHODS

No statistical methods were used to predetermine sample size. The experiments were not randomized and investigators were not blinded to allocation during experiments and outcome assessment.

Cryptotephra extraction methods. We collected samples at PP5-6 and VBB by sampling along excavated sections every centimetre, and measured with total stations that provided millimetre accuracy. A total station is a modern surveying instrument that integrates an electronic theodolite with an electronic distance meter. A theodolite uses a movable telescope to measure angles in both the horizontal and vertical planes. For VBB samples, we combined every 5 cm of sample because of small sample size. We integrated location data into an ArcGIS 10.3 (https://www.arcgis.com/) geo-database with other data, including plotted finds, OSL samples, micromorphology samples and stratigraphic observations. The archaeological excavation methods used have previously been described[8,21,22] as have the micromorphology methods[7]. In total, the samples and transects reported here from PP5-6 span the upper 1 m of LBSR, all of ALBS and the lower 60 cm of SADBS, where the shard count drops to zero. Natural variations in the slope and thickness of the sediments complicate linear 2D extrapolations of the sample locations within the sub-aggregates, so we calculated the relative height of each sample location above its nearest underlying sub-aggregate contact in each transect (Fig. 2): we also provide the raw shard counts per transect (Extended Data Figs 2, 3).

Because of the great travel distance, shards at PP5-6 and VBB are very rare and small. We label this type of tephra deposit, which is rarely found in complex archaeological sequences, extremely low abundance cryptotephra as a reflection of their low shard counts ($<$5 shards per gram) and small size ($<$50 μm). Extremely low abundance cryptotephra provide substantial processing and analytical challenges within cave and rock shelter sediments. Shards at VBB are fresh and provide excellent chemistry, but at PP5-6 they are altered and thus provide additional analytical challenges[6]. Separation of distal shards from sediment requires care and specialized techniques. In general, we followed a previously published method[10] designed for processing lacustrine and organic sediments, but modified the procedure as described below to process extremely low abundance cryptotephra. We conducted preliminary processing at Oxford University under the guidance of C. Lane, and performed subsequent processing at the University of Nevada, Las Vegas.

Samples were weighed to 1 g and placed in 50-ml centrifuge tubes. A 10% HCl solution was added to dissolve carbonates. The samples were subsequently sieved at 80 and 20 μm. The 80–20-μm sieve portion was further processed using lithium metatungstate heavy liquid at densities of 1.95 g per cm³ and 2.55 g per cm³, to separate the glass shards and other low-density grains. Samples were centrifuged twice at each density for 15 min at 2,500 r.p.m. After cleaning, the separate ($>$1.95 but $<$2.55 g per cm³) that contained shards was mounted on a one-inch diameter epoxy round suitable for both major- and trace-element analyses. For VBB, only grains identified chemically as shards were counted (see 'Cryptotephra analytical methods'). For PP5-6, grains were first mounted on petrographic slides for identification and counting. This count is reported as shards per gram of dried sediment and plotted against vertical position in the sediment column to construct shard frequency diagrams. Petrographic slides (for PP5-6) and epoxy rounds (for VBB) were ground and polished for geochemical analysis.

Cryptotephra analytical methods. Extremely low abundance cryptotephra from PP5-6 occur as plate-like, bubble-wall and blocky glass shards (Extended Data Fig. 1). Shard shape was difficult to quantify because shards were identified after being mounted in epoxy. Using this type of mount, only 2D sections of the shards were available, which precluded detailed shape analysis. Most PP5-6 samples contained abundant biogenic silica that has shapes similar to shards, as previously noted[23]. Biogenic silica was not present in the VBB samples but subangular-to-cuspate quartz was common. For VBB, only grains verified by chemical analysis were positively identified as shards. For PP5-6, 49 tephra shards were counted that could be confidently distinguished from biogenic silica under the microscope. Most shards in PP5-6 sediments were either too small for analysis, were lost during sample polishing or showed signs of alteration. Some shards are 40 μm in size, and polished surfaces available for analysis were usually much smaller. Many grains originally thought to be shards were analysed as biogenic opal. Because of these difficulties, we were only able to obtain major-element analyses from 3 shards from PP5-6 in samples 48, 49 and 125, and trace elements from samples 48 and 49. From VBB, we obtained eight major-element and five trace-element analyses (Fig. 4, Extended Data Figs 5, 6 and Extended Data Tables 1, 2).

The $<$40-μm shards were analysed for major and minor elements using a JEOL JSX8900 SuperProbe with four wavelength dispersive spectrometers. Analytical conditions for electron microprobe analysis were 10 nA current at 15 kV accelerating voltage using a 10-μm spot size. Peak and background counting times were 30 and 10 s, respectively. Peak and background counting times for Na were 10 and 5 s. The alkali elements Na and K were counted on the first wavelength

dispersive spectrometer cycle to minimize potential element migration from beam damage. The rhyolite glass standard ATHO-G, which is part of the MPI-DING international standard set[24], was used as an internal standard for all analyses. Analytical error for most elements is less than $\pm$0.2 weight per cent except SiO_2 ($\pm$0.83 weight per cent), Al_2O_3 ($\pm$0.25 weight per cent) and Na_2O ($\pm$0.57 weight per cent) (Supplementary Table 3).

Trace elements were obtained on a Thermo Scientific ICAP Q Quadrupole Inductively Coupled Plasma Mass Spectrometer (ICP-MS) at Michigan State University, in combination with a Photon Machines Analyte G2 193-nm excimer laser ablation system equipped with a 15× 15-cm HelEx sample cell for solid sample microanalyses. Parameters used were 4.1 J per cm² laser fluence at 10 Hz (that is, 10 laser hits per second each delivering 4.1 J per cm²). The sample cell was fluxed in He, which was also used as the carrier gas to the ICP-MS injector. The ICP-MS was tuned using laser ablation of glass standard NIST 612 with the same fluence and frequency, performing a surface scan, aiming for highest intensities while keeping oxide production rate (ThO/Th) $<$ 0.7% and double charged cations ($^{137}Ba^{++}/^{137}Ba$) $<$ 3%. Laser pit size was adjusted based on sample size, but tuning and calibration were done at a 110-μm pit diameter on surface scans of NIST 612, USGS basalt glass standards and rock powder standards from the Geological Survey of Japan and the US Geological Survey (Supplementary Table 4). Backgrounds were assessed by collecting a gas blank after each standard and sample, and backgrounds were automatically subtracted from each analysis. Samples and standards were mounted on the same tray, enabling continuous analysis. Data for the Geological Survey of Japan standard JB1-a are provided in Supplementary Table 4.

For PP5-6 shard 49, we used the Cameca IMS 6f Secondary Ionization Mass Spectrometer (SIMS) at Arizona State University. Instrumental parameters for SIMS were primary beam: $^{16}O^-$ at -12.5 kV, and current of 5 nA. Positive secondary ions were accelerated to 9,000 V into the mass spectrometer. Only secondary ions with 75 ± 20 eV excess kinetic energy were detected (conventional energy filtering). All ions were integrated for 5 s in each cycle of measurement, except for ^{30}Si, which was counted for 2 s in each cycle. Concentrations were determined by normalizing the secondary ion signal to that of ^{30}Si and referencing this ratio to the ion ratios previously determined on NIST 610 glass. The interference of BaO ions on Eu, NdO ions on Tb, NdO and SmO ions on Dy, SmO ions on Ho, NdO and SmO ions on Er, EuO ions on Tm, TbO ions on Lu, DyO ions on Hf and HoO ions on Ta were estimated using previously tabulated MO^+/M^+ values[25]. Errors are two standard errors of the mean of 10 cycles of measurement. Errors on elements that required oxide corrections were estimated to be 20–30% larger than the error on the uncorrected ion ratio. LA-ICP-MS was used on shards with sufficient thickness to produce a significant analysis. For thin grains, SIMS was the preferred method of analysis. Supplementary Table 5 contains the errors for each element.

To monitor instrument accuracy and precision, the secondary standard rhyolite glass ATHO-G, part of the MPI-DING standard set[24], was analysed alongside glass shards on the electron microprobe. The average of these analyses and the per cent relative standard deviation (%RSD), which is used as an indication of instrument precision, are provided in Supplementary Table 3. The average of analyses for standard JB1-a used for LA-ICP-MS and the errors for each element for SIMS analysis can be found in Supplementary Tables 4, 5.

Cryptotephra source identification. Even moderate-sized eruptions can produce tephra that travels long distances[26], so we searched records of known volcanism beyond Africa to Antarctica, South America and Indonesia. We limited our search to Southern Hemisphere and equatorial-belt volcanoes because inter-hemispheric transport of volcanic ash is uncommon. To account for possible reworking of older cryptotephra into younger deposits, we widened our time window to include eruptions from over 700 ka to the present, including tephra found within the Siple A ice core from west Antarctica[27], the Rungwe volcanic province in Tanzania[28], the Turkana basin in Kenya and Ethiopia, distal ash from Turkana region eruptions in the Gulf of Aden[29–31], the database of obsidian from Kenya[32], ash related to the Toba and Maninjau calderas in Indonesia[33,34] and volcanoes in the southern Andes in Chile and Argentina[35,36]. After this extensive search, we conclude that YTT is the source of the shards at both PP5-6 and VBB (see Supplementary Information for discussion).

Cryptotephra isochrons at PP5-6 and VBB. At PP5-6, the first appearance and highest concentration of shards occurs near the top of an aeolian sand unit (sub-aggregate Conrad Sand). This first peak is overlain by an approximately 10-cm-thick aeolian sand layer, which is free of shards, and then sealed by a series of successive intact hearth features also devoid of shards (in the lower Jocelyn sub-aggregate, Fig. 2). This confirms that wind-borne allochthonous material was able to enter the rock shelter at that time and that the first appearance of shards is a true isochron. The sand layer formed when the sea had regressed and the rock shelter opened onto a plain, providing a source for the wind-blown sand. A dune of similar age is found throughout Pinnacle Point and the shard input post-dates the beginning of this

dune activation. Such dunes move rapidly and can form thick sand layers within days. Above the hearth features, sub-aggregate Jocelyn shows a second increase in shards culminating within the overlying Erich sub-aggregate, both of which are located in sediments associated with trampled burnt remains[7]. These peaks and the overlying tail are interpreted to be reworkings of lateral exposures of the initial cryptotephra deposit by human trampling and continuous aeolian activity. We place the YTT isochron at the position of Conrad Sand (Fig. 2).

VBB has only a few shards in an aeolian deposit with extensive soil formation; placing an isochron there is challenging because the post-depositional migration of grains by mechanical and biological processes may mask the original position of the isochron. Bioturbation is especially common in sand dunes[37] and can cause grains to move down-section and even into units below the original depositional position. With the current results, we are not able to locate a more precise isochron in the VBB section. Although an isochron cannot be located, we do know that shards are found within and immediately above and below the SBCS unit dated to 74.7 ± 5.8 ka—a date that is nearly identical to the time of YTT ($\sim$74 ka)—and that the shards are an excellent match to the YTT chemistry.

Archaeological 3D density analysis methods. Stratigraphy at PP5-6 varies in both lateral and vertical morphology, which prevents simple 2D calculations of plotted-find point densities within these sediments. Therefore, we used ESRI ArcGIS 10.3 (https://www.arcgis.com/) to bin the plotted finds from the LBSR, ALBS and SADBS ($n = 117,975$) into 125-cm^3 cubes (5 cm × 5 cm × 5 cm) that were distributed evenly across the deposits in 3D space, using the South African National Grid (http://www.ngi.gov.za/index.php/technical-information/geodesy-and-gps/datum-s-and-coordinate-systems) (Lo. 23)) as input data. Counts of the points within each bin provided a standardized measure of 3D point density across the study deposits, at a resolution of 125 cm. Subsequent analyses were undertaken to assess the 3D density of points based on sub-aggregate and plotted find type (that is, stone artefact, bone, ochre and marine shell).

OSL methods. We have previously reported[15] 25 ages for sediment samples collected from PP5-6. These ages have now been re-analysed, refined and increased in number in our current and ongoing study, providing dates with improved precision that supersede the previously reported ages[15]. No significant changes in ages were obtained (that is, all ages changed within their reported uncertainties); the major change was due to the updates associated with beta dose attenuation factors (using the latest published[38] values, which also affect the dose rate of the 'Nussi' standard used in our beta counting estimates, and a change in the error calculation on our beta dose rates). Full details of these changes and their implications have previously been published[39].

To date, 90 samples have been collected for OSL dating from the entire excavated profile of PP5-6 (Supplementary Table 6). Our overarching aim is to bracket each stratigraphic aggregate (for example, ALBS), and—where possible—to date many of the sub-aggregates (for example, Conrad Sand in ALBS), to provide high-resolution OSL dating to match the contextual control provided through total station plotting, stratigraphy, 3D GIS of plotted finds and lenses, and micromorphology. This approach enables an assessment of temporal continuity (or lack thereof) between aggregates and estimate durations of specific lithic industries. Of particular use, the dense horizontal and vertical coverage of our ages can be input into a statistical age model for optimizing the resolution and precision of the chronology for the site. In this study, we use a Bayesian age model, using the OxCal platform (https://c14.arch.ox.ac.uk/oxcal.html), because this enables the relative stratigraphic information recorded at the site during excavation to be formally incorporated as a prior assumption in the model.

Experimental details are provided in a basic form: details of the chronology and associated methodological information have not yet been published, but the methods and handling of data are identical for every sample from PP5-6 and consistent with previously published methods[40,41].

OSL sample collection and preparation. We collected samples by driving a plastic tube ($\sim$1 cm in diameter, 20 cm long) into the cleaned section wall, or by using a cordless drill to loosen the samples (where necessary) and collecting the samples with a spoon at night using a red-filtered flashlight to ensure that sediments were collected from a single sub-aggregate. A sub-sample was also collected from the back of each hole for current soil moisture content measurements and for laboratory-based radioactivity measurements.

In the laboratory, the samples were opened under dim red illumination. Quartz grains of 180–212 μm in diameter were selected for dating, after purifying the samples using HCl, H_2O_2 and solutions of sodium polytungstate at specific densities of 2.62 and 2.70 to separate the quartz grains from the feldspar and heavy minerals, respectively. The quartz grains were then etched in hydrofluoric acid to remove the external alpha-dosed layer ($\sim$10 μm), and rinsed in HCl to dissolve any precipitated fluorides. The etched grains were sieved again to the lower sieve size (180 μm).

OSL equivalent dose determination. Equivalent dose (D_e) values were estimated for individual sand-sized grains from all samples. The measurement conditions and analytical procedures most appropriate for individual grains from Pinnacle Point have previously been established[41] and verified for the individual samples from PP5-6 through a range of dose recovery tests on representative samples from each of the stratigraphic aggregates. Measured dose:given dose ratios for these samples range between 0.97 ± 0.02 (sample 357332, aggregate OBS2) and 1.04 ± 0.04 (162516, RBSR), with overdispersion values of between 0% and $15 \pm 3\%$ and 1.01 ± 0.03 and overdispersion of $8 \pm 3\%$ for the sample from VBB (392138, SBCS). Overdispersion is the remaining amount of scatter after allowance is made for measurement uncertainties[42]. Because of this internal consistency, and because of the consistency between the VBB and PP5-6 samples and samples from other sites around Pinnacle Point, measurement and analytical procedures (including grain rejection, signal integration and preheat temperatures) were the same as previously used[41]. The equipment was also the same as that previously used[15,41]. By using the same methods, equipment, procedures and operator in all of the single-grain OSL dating studies at Pinnacle Point, we can now place PP5-6 and VBB on the common timescale developed for Pinnacle Point, which enables improved comparisons of ages within and between sites.

Information about the number of grains measured and used, their overdispersion values calculated and the final $D_e \pm 1\sigma$ value for each sample is presented in Supplementary Table 6. The central age model[42] was used to combine the individual single-grain D_e values of each sample to estimate the D_e for age calculation. The centre age model assumes that the D_e values for all grains are centred on some average value of D (similar to the median) and the estimated standard error takes any overdispersion into account. Overdispersion values for these samples range between 0% (46800 and 46789 in LBSR and DBCS, respectively) and $35 \pm 4\%$ (418198 in ALBS) and, for samples from VBB, between $23 \pm 5\%$ and $30 \pm 6\%$ (Supplementary Table 6). Where overdispersion values are larger than expected, it is mostly due to one or two extreme outliers (see previously published plots[15]). All grains, regardless of whether they are extreme outliers or not, were included in the weighted mean value in case they form part of the natural variability of these samples. The weighted mean is insensitive to their inclusion.

OSL dose rate determination. The total dose rate consists of contributions from beta, gamma and cosmic radiation external to the grains, plus a small alpha dose rate due to the radioactive decay of U and Th inclusions inside sand-sized grains of quartz. To calculate the OSL ages, we have assumed that the measured radionuclide activities and dose rate have prevailed throughout the period of sample burial. An internal alpha dose rate of 0.036 ± 0.01 Gy ka^{-1} has been assumed for all samples, based on measurements made on samples from the nearby site of Blombos Cave[43].

Bulk beta dose rates were measured directly by low-level beta counting of dried, homogenized and powdered sediment samples in the laboratory, using a GM-25-5 multi-counter system[44]. The beta dose rate procedures used here have been shown to be both accurate and reproducible using a range of independent measurement techniques, with measurements performed in-house and by external laboratories[40]. In this study, we have updated our previously published beta dose rate[15], re-measured a selection of the samples, used the latest conversion factors and reassessed the errors associated with our beta dose rates, following the worked example[39] provided in Supplementary Information.

Gamma dose rates were measured at each sample location by *in situ* gamma spectrometry to take account of any spatial heterogeneity in the gamma radiation field within 30 cm of each OSL sample (as gamma rays can penetrate this distance through sediment and rock). Counts were collected for at least 60 min with a 1-inch Na(Tl) crystal. The detector was calibrated using the concrete blocks at Oxford[45] and the gamma dose rate was determined using the 'threshold' technique[46]. This approach gives an estimate of the combined dose rate from gamma-ray emitters in the U and Th chains and from ^{40}K.

The cosmic-ray contribution was also taken into account, adjusting for site altitude, geomagnetic latitude, the density and thickness of rock and sediment overburden[47], and the $\cos^2$-Φ zenith angle dependence of cosmic rays[48]. We used the 3D GIS developed for PP5-6 as an aid to obtain accurate estimates of the various parameters that are input into the equation for estimating the cosmic-ray dose rate[21] and considered the changes in dripline based on sedimentological observations to make informed decisions about the long-term patterns in rock overburden.

The beta, gamma and cosmic-ray dose rates were corrected for long-term water contents. The sandy layers and roofspall-rich layers are generally very dry, whereas those layers that contain substantial amounts of ash tend to be wetter. We assumed that this difference has always been the case. We used the current moisture contents as a guide and assigned a relative uncertainty of $\pm 25\%$ (at 1σ) to each estimate, unless it is a very low content, in which case an absolute error of $\pm 1\%$ was assigned (for example, $3 \pm 1\%$). At VBB, the current moisture content estimates

were generally very dry (<3%), so we have used a consistent value of $5\pm2\%$ for all samples. We think that this accommodates any likely variations over the average burial period of these samples. As a general rule of thumb for quartz grains, a 1% increase in water content will lead to an approximately 1% increase in age.

Statistical methods. *Cryptotephra.* Major element data from five volcanic fields (Maninjau, Andes Pat (Patagonia), Turkana, Antarctica and Rungwe) and six positively identified YTT distal samples (Malaysia, Lake Malawi, South China Sea, Bay of Bengal, Arabian Sea and India) were used as reference data for comparisons with unknown samples from PP5-6 and VBB. In this analysis, the six YTT distal datasets are combined into a single group within the major element analysis. Here we refer to the dataset of each volcanic field as a 'site'. We included 10 major elements from 791 samples from these sites (Supplementary Table 8a). Additionally, 25 trace elements from 333 samples from the following six sites were also included in the statistical analysis: Antarctica–Vostok, Kenya obsidian, Maninjau, Rungwe, Turkana and the YTT in Malaysia (Supplementary Table 8a). References for published data are included in the Supplementary Information. All data were log-transformed and standardized by subtracting their mean and dividing by the standard deviation. The element data were used to construct a Bayesian probability model, which assimilated the 10 variables associated with the major-element analysis and the 25-trace-element analysis (that is, two separate analyses were performed using the 10 major elements and the 25 trace elements). The full probability model describes the dependences among the data and parameters that produce posterior distributions: $P(\mu, \Sigma, p|C) \propto P(C|\mu, \Sigma)P(\mu)P(\Sigma)$. We assume the continuous trait data (major or trace element data), C, arise from a multivariate normal distribution. A mean vector μ and covariance matrix Σ describe the covariation among quantitative traits. The mean variable vector μ is assumed to vary by site (s) (for example, Antarctica, Rungwe). Thus, for the observation $i = 1, 2,…, n, C = 1, 2, …, C$ quantitative traits and sites $s = 1, 2, …, 6$, $P(C|\mu, \Sigma)$ is given as

$$\begin{pmatrix} C_{1,i} \\ C_{2,i} \\ C_{n,i} \end{pmatrix} \sim \text{Normal} \left(\begin{pmatrix} \mu_{1,s} \\ \mu_{3,s} \\ \mu_{n,s} \end{pmatrix}, \Sigma \right)$$

We chose relatively non-informative conjugate priors for all quantities. An uninformative normal (Normal (0,10000) prior was specified for each component of μ and a relatively non-informative Wishart (R, k) prior[49] was chosen for the precision matrix $(\Omega = \Sigma^{-1})$, with $k = 10$ degrees of freedom and R as a 10×10 matrix.

The Bayesian model was implemented in OpenBUGS, a Bayesian simulation software[50]. OpenBUGS uses Markov chain Monte Carlo (MCMC) routines to sample from the joint posterior distribution, enabling the generation of approximations of posterior distributions. Three parallel MCMC chains were run for 150,000 iterations and chains converged for all parameters and showed good mixing by 50,000 iterations. After thinning by 10 to reduce autocorrelation, a total of 30,000 iterations was used to calculate posterior statistics including the mean and 95% credible interval, defined by the 2.5th and 97.5th percentiles of each marginal posterior distribution.

We tested the predictive ability of our two models by randomly dividing our reference dataset of known volcanic eruptions into two subsets, 'training' data (90%) and 'validation' data (10%), to perform an out-of-sample cross validation. Each major- and trace-element dataset was subdivided into 'training' and 'validation' data subsets. For each dataset, 10% of the data was randomly assigned 'not assigned' (NA) for the variable 'site' (s). For every 'NA' sample, the model assigns the sample as belonging to each site with a given probability. A prior for the variable s is assigned as a categorical distribution with equal probability ($P_i = 0.1667$) for each of the six possible sites, using the equation $s_i \sim \text{categorical}(P_i)$. Drawing from the training data, the model thus assigns each 'unknown' sample a value for s. On completion of the out-of-sample cross validation, training and data subsets were recombined and used to analyse the archaeological samples from PP5-6 and VBB.

After removing the burn-in period ('burn-in' refers to the initial number of MCMC iterations before chain convergence), our model predicted the site of each 'unknown sample'. Accurate assignment of site was determined according to the highest probability of assignment. Values represent the proportion of MCMC iterations that assigned each sample to each respective site. For example, observation 18 (Supplementary Table 9, first entry) derives from the site Andes Pat. Drawing from distributions of major element data, the Bayesian model accurately assigned the sample with 100% probability. By contrast, the model incorrectly assigned observation 21 (Supplementary Table 9, second entry) from Andes Pat as Toba with 65% probability.

The results of the out-of-sample cross validation for the major element model suggest the model predicts at 92.4% accuracy (Supplementary Table 9); that is, the model accurately predicted the site for 'unknown' (samples known to the analyst but blind to the model) approximately 91.3% of the time. Six misidentified samples

were incorrectly assigned as Maninjau. Similarly, the model accurately differentiated sites using only trace element data with 79.4% accuracy (Supplementary Table 10). In contrast to the model using major element data, misidentified samples were likely to be assigned across multiple sites with equal probabilities rather than mis-assigned as a single site with high probability.

On assessing model performance, training and validation subsets were recombined and used to predict archaeological samples. Within the major element model, three samples derive from PP5-6 and seven samples derive from VBB. The major element model predicted both PP5-6 and VBB samples to belong to the Toba group with high probability (Extended Data Table 3). Similarly, the trace element model included two samples from PP5-6 and six samples from VBB, each predicted to belong to Toba with high probability (Extended Data Table 4).

OSL. Our single-grain OSL dates were put into a Bayesian statistical model on the OxCal platform (OxCal 4.2)[51,52]. The dating estimates (Supplementary Table 6) were input as 'C_' dates in calendar years before present, with an associated 1σ error. The OSL ages reported include both the random and systematic uncertainties. When ages with common systematic errors and random errors are combined, only the latter should be included. Therefore, we excluded all systematic errors[53] before constructing the Bayesian model; 'random-only' errors are shown in parentheses in the 'age' column of Supplementary Table 6.

To maximize the information that we obtained from the OSL dates for PP5-6, we used as prior information 10 of the 12 major stratigraphic aggregates. We did not include YBS because we only had one age for this unit; we included this age in YBSR. We also omitted the DBCS, which is a complex sedimentary unit that consists of sediment derived through debris flow from more than one stratigraphic aggregate (BBCSR and OBS2)[7]. We also used our knowledge regarding the relative stratigraphic position of each of the sub-aggregates that together make up the stratigraphic aggregates. We were therefore able to place our ages into sequences using the fine-scale stratigraphic information within each of the stratigraphic aggregates: we know, for example, that 'Conrad Cobble and Sand' in ALBS predates Conrad Sand and must therefore be older. Where we had more than one age estimate from a single sub-aggregate, we placed them into phases within the sequence, so that there were no assumptions about the relative order of the samples within the sub-aggregate.

We also used the outlier detection analysis[54] to assess the likelihood of each result being consistent within the constraints of the modelled sequence; this enables identification of possible erroneous ages. During the modelling process, the posterior outlier probability is calculated and the date down-weighted accordingly. For example, if the posterior probability is found to be 5%, the date is included in 95% of the model iterations, but if it is found to be 50% it is included in only 50% of model iterations. The outlier analysis detected seven significant outliers: specimen number 162660 (Aaron Sand and Roofspall), 418195 (Lwando Sand and Roofspall) and 110634 (Ludumo Sand and Roofspall) in LBSR, 418199 (Conrad Cobble and Sand) in ALBS, 357343 (Chris/Orfer) in OBS1, 357338 (Zuri Upper) in SGS and 162515 (Denise) in RBSR. This amounts to around 8%, which is slightly higher than statistical expectations (1 in 20 at 2σ).

The Bayesian age model for the samples from PP5-6 is shown in Fig. 2. The measured OSL ages are shown as black filled circles with their 1σ (68.2% probability) error bars, assuming a Gaussian distribution. The modelled ages are shown in orange as a continuous age range. These modelled age ranges are at 2σ (95.4% probability). The modelled probability distribution functions for the stratigraphic aggregate boundaries are also shown. Modelled age ranges are provided in Supplementary Table 6 and the stratigraphic aggregate boundaries are in Supplementary Table 7.

Sensitivity tests of the model have been conducted. The model was run four times using at least 50 million iterations and we confirmed that the modelled age estimates and posterior distribution functions for the stratigraphic boundaries were reproducible and that convergence values were high.

Code availability. The Bayesian age model coding is provided in the Supplementary Information.

Data availability. Most data generated or analysed during this study are included in the article and its Supplementary Information. All other data are available from the corresponding authors on reasonable request.

23. Visser, M. P. E. *Detection of Middle to Late Holocene Icelandic Cryptotephra in the Netherlands: Tephra versus Biogenic Silica*. MSc thesis, Univ. Utrecht (2012).
24. Jochum, K. P. *et al.* MPI-DING reference glasses for *in situ* microanalysis: new reference values for element concentrations and isotope ratios. *Geochem. Geophys. Geosyst.* **7,** Q02008 (2006).
25. Zinner, E. & Crozaz, G. A method for the quantitative measurement of rare earth elements in the ion microprobe. *Int. J. Mass Spectrom.* **69,** 17–38 (1986).
26. Jensen, B. J. L. *et al.* Transatlantic distribution of the Alaskan White River Ash. *Geology* **42,** 875–878 (2014).

27. Dunbar, N. W. & Kurbatov, A. V. Tephrochronology of the Siple Dome ice core, West Antarctica: correlations and sources. *Quat. Sci. Rev.* **30,** 1602–1614 (2011).
28. Fontijn, K. *et al.* Holocene explosive eruptions in the Rungwe Volcanic Province, Tanzania. *J. Volcanol. Geotherm. Res.* **196,** 91–110 (2010).
29. Feakins, S. J., Brown, F. H. & deMenocal, P. B. Plio-Pleistocene microtephra in DSDP site 231, Gulf of Aden. *J. Afr. Earth Sci.* **48,** 341–352 (2007).
30. Brown, F. H., Haileab, B. & McDougall, I. Sequence of tuffs between the KBS Tuff and the Chari Tuff in the Turkana Basin, Kenya and Ethiopia. *J. Geol. Soc. London* **163,** 185–204 (2006).
31. Haileab, B. *Geochemistry, Geochronology and Tephrostratigraphy of Tephra from the Turkana Basin, Southern Ethiopia and Northern Kenya.* Ph.D. thesis, Univ. Utah (1995).
32. Brown, F. H., Nash, B. P., Fernandez, D. P., Merrick, H. V. & Thomas, R. J. Geochemical composition of source obsidians from Kenya. *J. Archaeol. Sci.* **40,** 3233–3251 (2013).
33. Chesner, C. A. & Luhr, J. F. A melt inclusion study of the Toba Tuffs, Sumatra, Indonesia. *J. Volcanol. Geotherm. Res.* **197,** 259–278 (2010).
34. Hashim, N. B. *Time Marker for the Late Pleistocene in Peninsular Malaysia: Study of the Volcanic Ash Deposits.* MSc thesis, Univ. Malaysia (2014).
35. Weller, D. J., Miranda, C. G., Moreno, P. I., Villa-Martínez, R. & Stern, C. R. Tephrochronology of the southernmost Andean Southern Volcanic Zone, Chile. *Bull. Volcanol.* **77,** 107 (2015).
36. Hildreth, W., Fierstein, J., Godoy, E., Drake, R. & Singer, B. The Puelche Volcanic Field: extensive Pleistocene rhyolite lava flows in the Andes of central Chile. *Rev. Geol. Chile* **26,** http://dx.doi.org/10.4067/S0716-02081999000200008 (1999).
37. Ahlbrandt, T. S., Andrews, S. & Gwynne, D. T. Bioturbation in eolian deposits. *J. Sediment. Res.* **48,** 839–848 (1978).
38. Guérin, G., Mercier, N., Nathan, R., Adamiec, G. & Lafrais, Y. On the use of the infinite matrix assumption and associated concepts: a critical review. *Radiat. Meas.* **47,** 778–785 (2012).
39. Jacobs, Z. & Roberts, R. G. An improved single grain OSL chronology for the sedimentary deposits from Diepkloof Rockshelter, Western Cape, South Africa. *J. Archaeol. Sci.* **63,** 175–192 (2015).
40. Jacobs, Z., Roberts, R. G., Nespoulet, R., El Hajraoui, M. A. & Debénath, A. Single-grain OSL chronologies for Middle Palaeolithic deposits at El Mnasra and El Harhoura 2, Morocco: implications for Late Pleistocene human–environment interactions along the Atlantic coast of northwest Africa. *J. Hum. Evol.* **62,** 377–394 (2012).
41. Jacobs, Z. An OSL chronology for the sedimentary deposits from Pinnacle Point Cave 13B—a punctuated presence. *J. Hum. Evol.* **59,** 289–305 (2010).
42. Roberts, R. G., Galbraith, R. F., Olley, J. M., Yoshida, H. & Laslett, G. M. Optical dating of single and multiple grains of quartz from Jinmium Rock Shelter, Northern Australia: part II, results and implications. *Archaeometry* **41,** 365–395 (1999).
43. Jacobs, Z., Wintle, A. G. & Duller, G. A. T. Optical dating of dune sand from Blombos Cave, South Africa: I—multiple grain data. *J. Hum. Evol.* **44,** 599–612 (2003).
44. Bøtter-Jensen, L. & Mejdahl, V. Assessment of beta dose-rate using a GM multicounter system. *Radiat. Meas.* **14,** 187–191 (1988).
45. Rhodes, E. J. & Schwenninger, J.-L. Dose rates and radioisotope concentrations in the concrete calibration blocks at Oxford. *Anc. TL* **25,** 5–8 (2007).
46. Mercier, N. & Falgueres, C. Field gamma dose-rate measurement with a NaI (Tl) detector: re-evaluation of the 'threshold' technique. *Anc. TL* **25,** 1–4 (2007).
47. Prescott, J. R. & Hutton, J T. Cosmic ray and gamma ray dosimetry for TL and ESR. *Int. J. Rad. Appl. Instrum. D* **14,** 223–227 (1988).
48. Smith, M. A., Prescott, J. R. & Head, J. N. Comparison of ^{14}C and luminescence chronologies at Puritjarra rock shelter, central Australia. *Quat. Sci. Rev.* **16,** 299–320 (1997).
49. Gelman, A. *et al. Bayesian Data Analysis* (CRC, 2013).
50. Lunn, D., Spiegelhalter, D., Thomas, A. & Best, N. The BUGS project: evolution, critique and future directions. *Stat. Med.* **28,** 3049–3067 (2009).
51. Ramsey, C. B. Development of the radiocarbon calibration program. *Radiocarbon* **43,** 355–363 (2001).
52. Ramsey, C. B. Bayesian analysis of radiocarbon dates. *Radiocarbon* **51,** 337–360 (2009).
53. Rhodes, E. J. *et al.* Bayesian methods applied to the interpretation of multiple OSL dates: high precision sediment ages from Old Scatness Broch excavations, Shetland Isles. *Quat. Sci. Rev.* **22,** 1231–1244 (2003).
54. Ramsey, C. B. Dealing with outliers and offsets in radiocarbon dating. *Radiocarbon* **51,** 1023–1045 (2009).
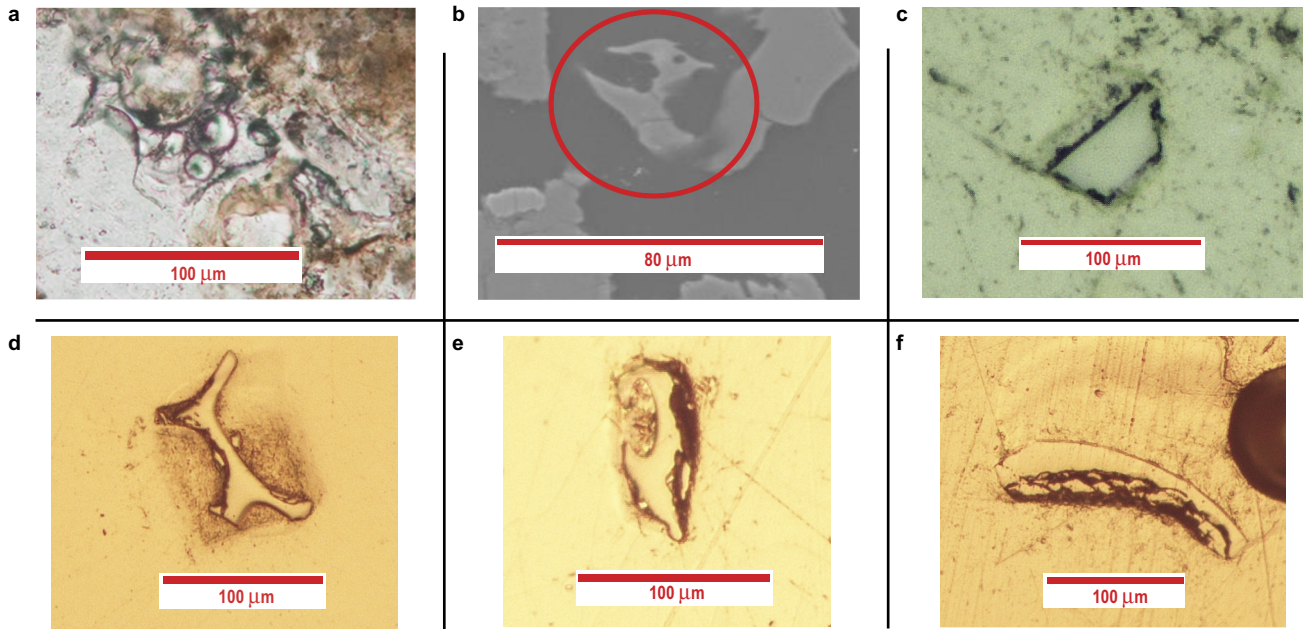
Extended Data Figure 1 | Examples of VBB and PP5-6 extremely low abundance cryptotephra. a, Two shard-like grains from PP5-6 in thin section (originally discovered by P.K.). **b**, Shard from PP5-6 sample 48 (scanning electron microscopy image). **c**, Shard from PP5-6 sample 125 (in thin section using plane-polarized light). **d**–**f**, Shards from VBB (from polished epoxy rounds using plane-polarized light).
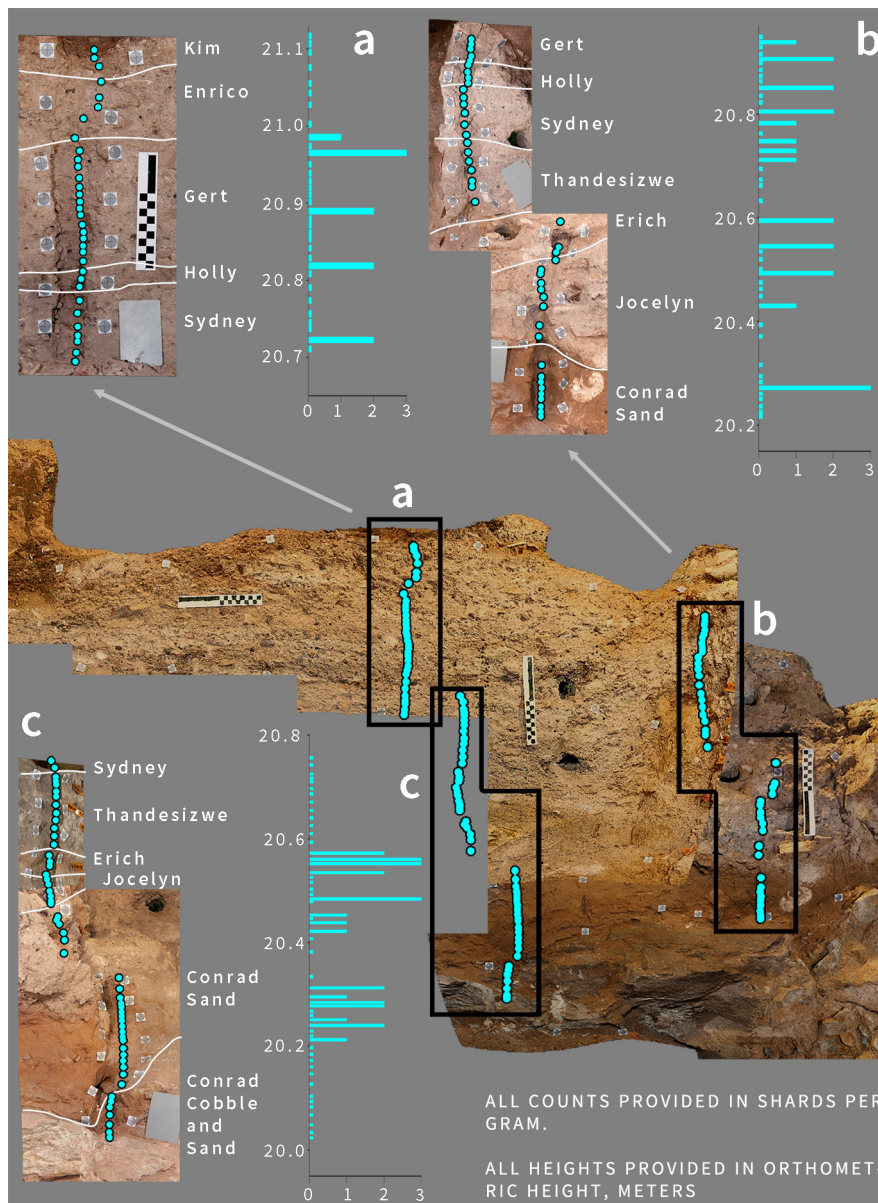
Extended Data Figure 2 | Individual sample transects on the sections and the shard counts from the transect. Sample transects are shown on the left and shard counts are shown on the right. **a**, Transect A. **b**, Transect B. **c**, Transect C. The small bars showing shard counts of less than 1 indicate a sample with no shards. See Extended Data Fig. 4 for the overall location of the transects relative to one another.
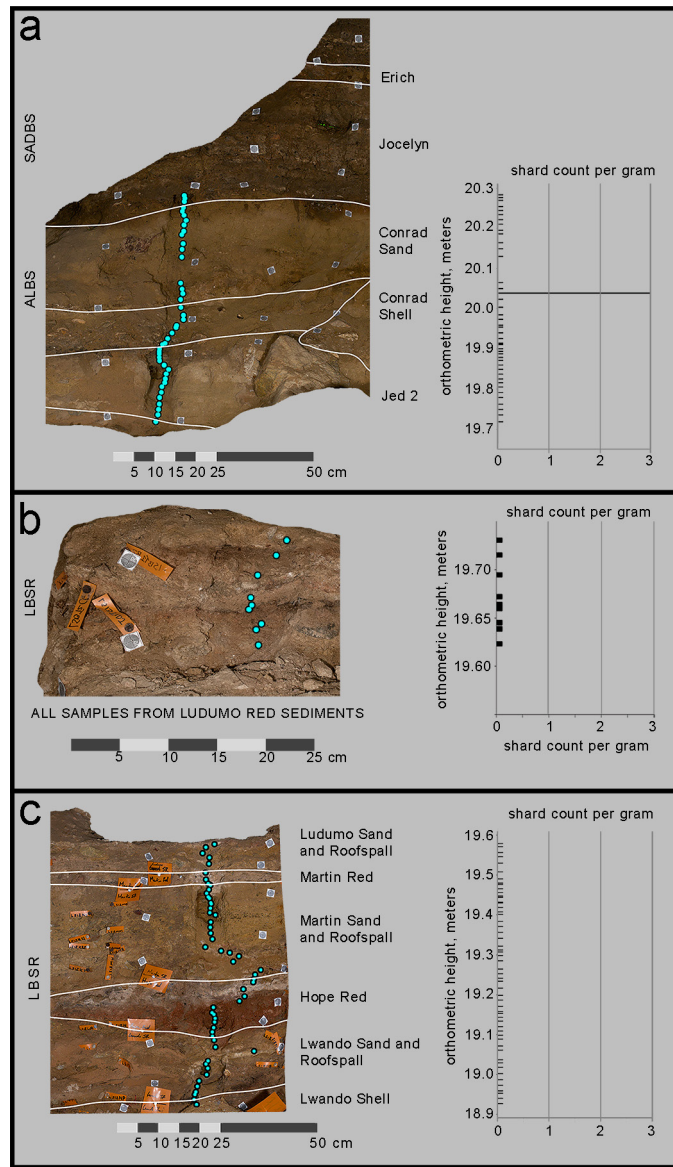
Extended Data Figure 3 | Individual transects on the sections and the shard counts per transect. a, Transect D. **b**, Transect E. **c**, Transect F. Transects are shown on the section (left), and shard counts per transect plotted (right). The small bars showing shard counts of less than 1 indicate a sample with no shards. See Extended Data Fig. 4 for the overall location of the transects relative to one another.
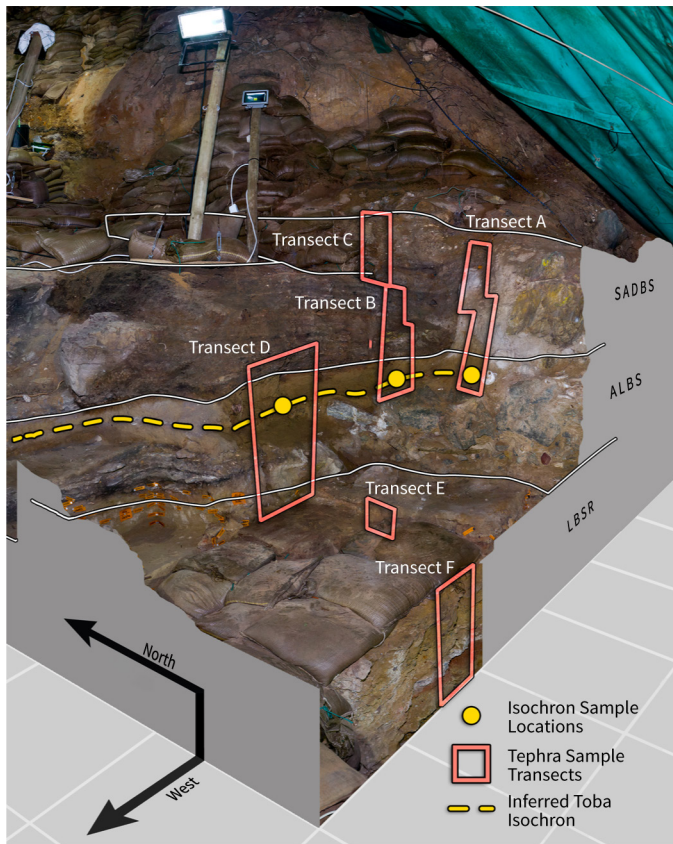
Extended Data Figure 4 | Panoramic photograph showing zones of contact between LBSR, ALBS and SADBS, and the location of shard sample transects. White lines indicate boundaries between stratigraphic aggregates and the yellow line indicates the YTT isochron.
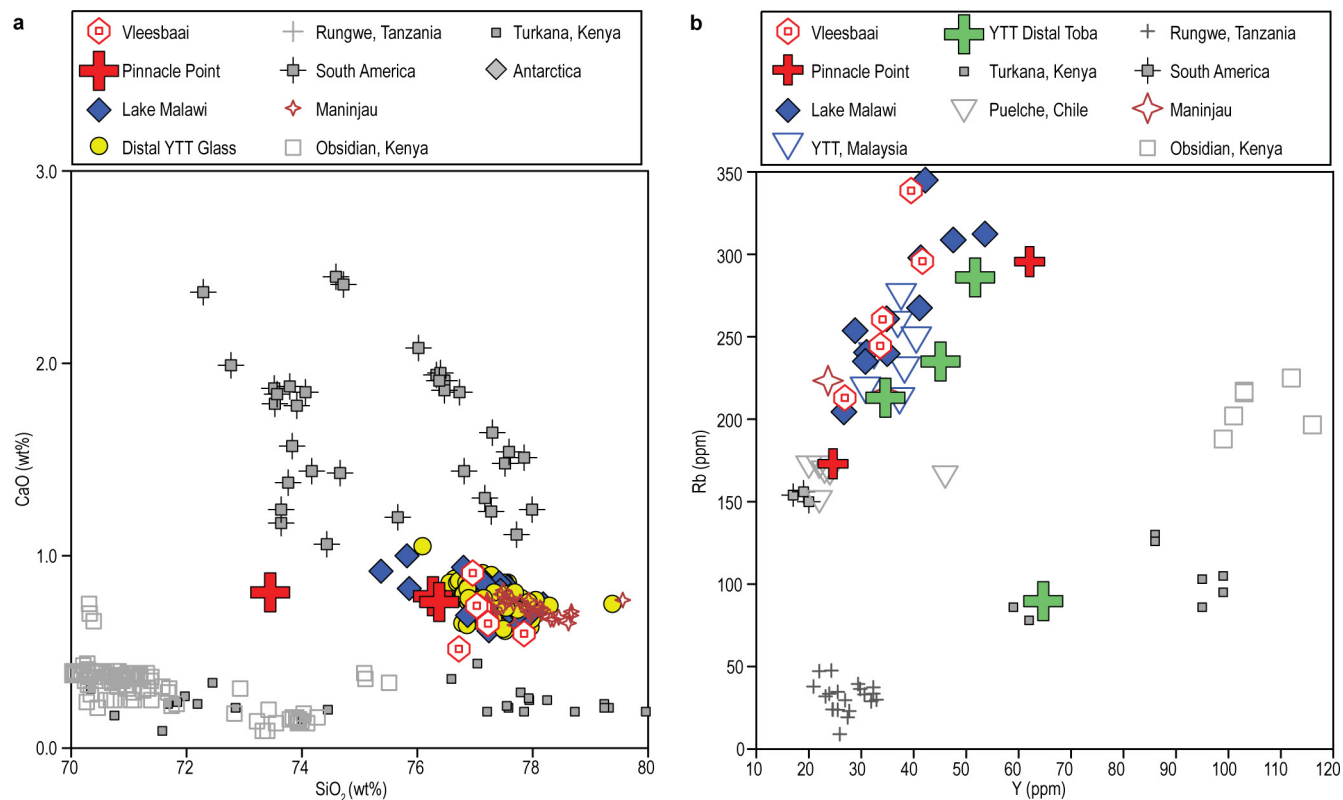
Extended Data Figure 5 | Geochemical comparisons between the VBB and PP5-6 extremely low abundance cryptotephra and distal and proximal YTT. a, CaO versus SiO_2 (wt%). **b**, Rb versus Y (parts per million, p.p.m.). Note the change in symbols between **a** and **b** to separate YTT distal glass from Toba caldera and Malaysian samples.
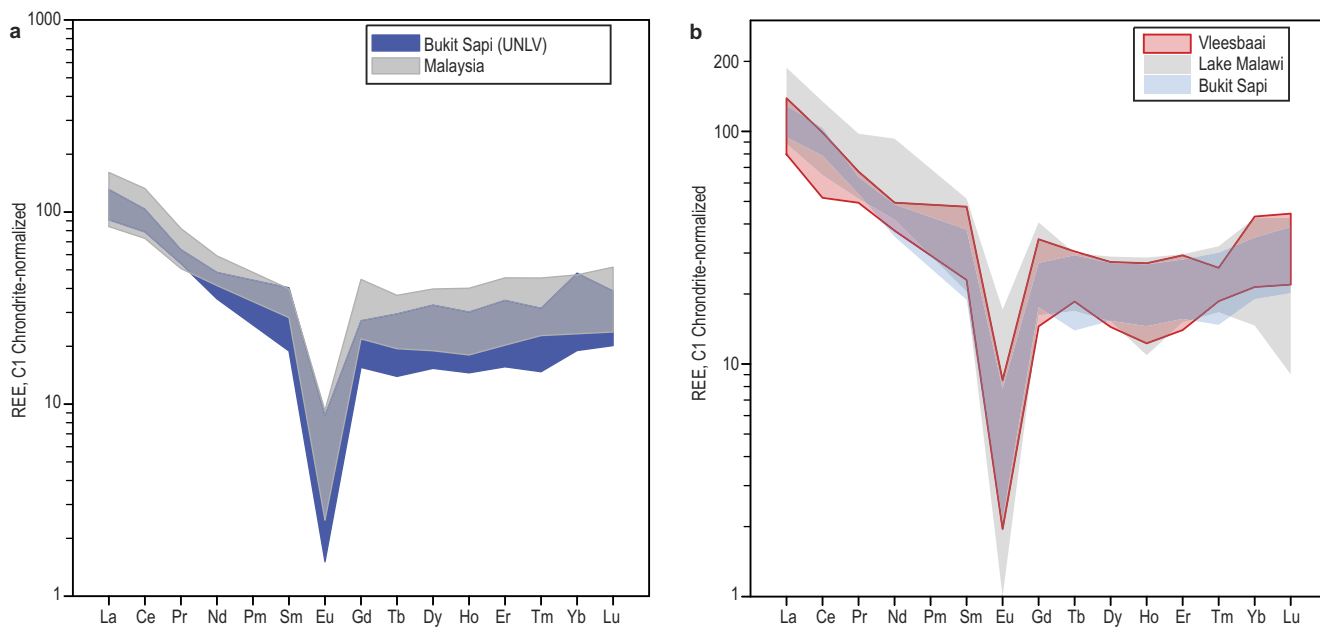
Extended Data Figure 6 | Comparison of trace-element chemistry. a, Rare-earth element plot comparing new data for YTT from Bukit Sapi (Supplementary Table 1) to previously published data[34]. **b**, Comparison of rare-earth element data for VBB, YTT from Lake Malawi and Bukit Sapi.

Extended Data Table 1 | Comparison of VBB, PP5-6, Lake Malawi, Bukit Sapi and Toba caldera shard analyses

	VBB (8)*	STDEV**	PP5-6 (3)	STDEV	Lake Malawi (18)	STDEV	Bukit Sapi (31)	STDEV	Toba Caldera (118)	STDEV
SiO_2	77.20	0.34	75.37	1.66	77.24	1.79	77.46	1.16	77.22	0.70
TiO_2	0.05	0.08	0.21	0.10	0.05	0.04	0.05	0.05	0.06	0.06
Al_2O_3	12.41	0.23	13.57	1.88	12.41	0.31	12.33	0.29	12.54	0.39
FeO	0.81	0.07	1.29	0.39	0.84	0.14	0.90	0.34	0.85	0.24
MnO	0.07	0.03	0.09	0.03	0.07	0.08	0.06	0.08	0.07	0.09
MgO	0.06	0.03	0.08	0.07	0.05	0.06	0.06	0.06	0.05	0.04
CaO	0.70	0.12	0.79	0.03	0.77	0.19	0.78	0.09	0.78	0.21
Na_2O	3.23	0.29	2.90	0.54	2.95	0.37	3.05	0.19	3.10	0.34
K_2O	5.17	0.24	5.33	0.40	5.61	0.45	5.31	0.41	5.20	0.29
P_2O_5	0.01	0.01	0.05	0.04	N.A.	N.A.	N.A.	N.A.	N.A.	N.A.

Trace elements in ppm	MSU***		MSU, ASU#		MSU (14)		MSU (12)		Toba Glass from Westgate et al. (13)			
Ga	11.60	4.22	N.A.	N.A.	16.10	5.87	14.57	2.57	N.A.	N.A.	N.A.	N.A.
Rb	254	59.84	296	0.00	264	34.34	279	35.57	286 ± 34	253 ± 26	235 ± 31	213 ± 28
Sr	35.56	16.88	37.95	7.00	48.36	20.25	36.26	12.55	28.5 ± 4.9	56.2 ± 8.0	75.8 ± 13.5	108.0 ± 14.9
Y	31.64	10.02	43.35	26.52	37.51	6.73	36.42	7.41	64.7 ± 10.7	51.7 ± 10.3	45.1 ± 10.0	34.6 ± 5.5
Zr	79.34	11.19	278	46.67	81.90	19.35	81.37	11.08	108 ± 16	112 ± 16	122 ± 21	128 ± 18
Nb	16.70	2.50	51.60	25.60	18.23	6.19	17.16	2.29	22.5 ± 2.5	18.9 ± 2.2	17.8 ± 2.1	16.4 ± 1.7
Cs	10.19	3.22	N.A.	N.A.	11.09	2.38	11.31	2.42	N.A.	N.A.	N.A.	N.A.
Ba	231	21.43	241	4.24	356	65.38	283	183.28	88 ± 23	382 ± 54	737 ± 145	1142 ± 104
La	24.35	4.93	76.60	10.75	29.00	6.08	25.18	3.08	32.3 ± 4.3	36.9 ± 5.4	43.9 ± 7.3	60.7 ± 11.2
Ce	45.95	10.23	147	26.87	59.09	13.29	54.83	4.36	62 ± 6.5	67.4 ± 7.6	74.3 ± 8.6	99.2 ± 13.2
Pr	5.23	0.86	16.45	3.32	6.32	0.92	5.53	0.32	7.42 ± 1.05	7.70 ± 1.21	8.55 ± 1.56	10.12 ± 1.45
Nd	18.97	2.78	50.05	3.04	22.45	3.39	19.00	1.73	28.1 ± 4.5	28.4 ± 6.2	29.7 ± 6.1	34.4 ± 5.7
Sm	4.37	1.85	7.40	1.56	4.77	1.45	4.23	1.02	7.43 ± 1.63	6.66 ± 1.52	6.52 ± 1.91	6.36 ± 2.92
Eu	0.26	0.13	0.69	0.13	0.43	0.19	0.29	0.12	0.32 ± 0.27	0.44 ± 0.26	0.59 ± 0.37	0.74 ± 0.32
Gd	4.15	1.62	4.51	0.00	4.85	0.87	4.18	0.78	7.95 ± 2.25	6.91 ± 2.43	6.61 ± 2.40	5.59 ± 1.98
Tb	0.73	0.24	0.82	0.00	0.76	0.15	0.77	0.20	1.42 ± 0.32	1.21 ± 0.35	1.07 ± 0.34	0.88 ± 0.27
Dy	4.64	1.60	3.94	0.37	5.33	1.12	5.35	1.32	9.64 ± 2.06	7.91 ± 1.90	7.37 ± 2.20	5.53 ± 1.49
Ho	0.93	0.38	0.83	0.04	1.11	0.24	1.15	0.26	2.17 ± 0.46	1.82 ± 0.48	1.62 ± 0.47	1.26 ± 0.37
Er	3.09	1.25	2.67	0.38	3.34	0.85	3.70	0.90	6.99 ± 1.40	5.78 ± 1.67	5.15 ± 1.66	3.93 ± 1.00
Tm	0.48	0.20	0.47	0.05	0.62	0.19	0.57	0.14	1.18 ± 0.28	0.97 ± 0.27	0.84 ± 0.29	0.65 ± 0.21
Yb	4.34	1.88	2.71	0.01	4.13	1.28	4.58	1.33	7.96 ± 1.35	6.30 ± 1.13	5.74 ± 1.44	4.26 ± 0.93
Lu	0.71	0.26	0.40	0.00	0.63	0.20	0.65	0.15	1.28 ± 0.27	1.01 ± 0.28	0.92 ± 0.28	0.69 ± 0.18
Hf	3.09	0.78	5.82	2.72	2.76	0.83	3.15	0.39	5.47 ± 1.22	5.02 ± 1.06	5.16 ± 1.19	5.08 ± 1.17
Ta	1.96	0.53	2.13	0.25	1.77	0.48	2.08	0.35	3.48 ± 0.57	2.72 ± 0.43	2.45 ± 0.47	1.95 ± 0.34
Pb	34.20	3.86	27.30	3.11	32.50	4.42	38.35	2.90	59.9 ± 18.6	60.7 ± 12.5	58.3 ± 16.5	59.8 ± 12.8
Th	30.86	9.21	14.10	1.84	29.76	7.35	32.58	4.71	58 ± 8.9	48.8 ± 7.9	45.5 ± 8.3	40.5 ± 5.9
U	5.72	1.27	3.80	0.42	4.56	1.32	5.35	0.99	9.97 ± 1.44	7.55 ± 0.99	6.34 ± 1.09	5.30 ± 0.66

Numbers in parentheses are sample sizes. N.A., not applicable.

*UNLV EPMA, analysis by electron probe microanalysis at the University of Nevada Las Vegas.

**STDEV, two standard deviations.

***MSU, analysis by LA-ICP-MS at Michigan State University.

#ASU, analysis by SIMS at Arizona State University.

Extended Data Table 2 | Major and minor trace element chemistry for VBB and PP5-6

Major Elements in wt% by EPMA

	VBB VBB6	VBB VBB6-2	VBB VBB16-1	VBB VBB16-2	VBB VBB9	VBB VBB8	VBB VBB-7-2	VBB VBB12-2	PP5-6 PP125	PP5-6 PP49	PP5-6 PP48
SiO_2	76.96	77.41	77.09	77.03	77.23	77.85	76.72	77.32	76.27	76.38	73.45
TiO_2	0.02	0.07	0	0.21	0.01	0	0.11	0	0.12	0.18	0.32
Al_2O_3	12.4	12.35	12.49	12.82	12	12.27	12.46	12.49	12.68	12.3	15.73
FeO	0.85	0.85	0.88	0.81	0.79	0.66	0.77	0.89	0.85	1.61	1.41
MnO	0.08	0.06	0.07	0.01	0.05	0.1	0.06	0.11	0.11	0.05	0.11
MgO	0.05	0.06	0.04	0.08	0.11	0.04	0.03	0.05	0.04	0.04	0.16
CaO	0.91	0.82	0.73	0.74	0.65	0.6	0.52	0.66	0.79	0.76	0.81
Na_2O	3.18	3.03	3.54	2.91	3.19	3.5	3.62	2.89	3.43	2.92	2.36
K_2O	4.98	5.07	4.92	5.21	5.3	4.99	5.66	5.19	5.51	5.6	4.87
P_2O_5	0.04	0	0	0	0	0	0	0	0.07	0	0.07
F	0.2	0.13	0.03	0	0	0	0	0.26	0	0.01	0.61
Cl	0.43	0.2	0.18	0.19	0.18	0.08	0.01	0.15	0.14	0.15	0.17
Original Total	96.43	97.33	94.84	95.41	95.14	94.93	100.12	96.68	94.04	96.11	92.95

Trace Elements in ppm by LA-ICP-MS, PP49 by SIMS

	VBB6	VBB6-2	VBB16-1	VBB16-2	VBB9	VBB8	VBB-7-2	VBB12-2	PP125	PP49	PP48
Ga	13.22	17.87	9.44	12.88	10.9	5.26	N.A.	N.A.	N.A.	N.A.	N.A.
Rb	260.5	169.3	295.8	212.9	338.6	244.5	N.A.	N.A.	N.A.	296.0	296.0
Sr	52.94	51.54	15.64	47.59	23.52	22.13	N.A.	N.A.	N.A.	33	42.9
Y	34.07	14.12	41.66	26.86	39.5	33.62	N.A.	N.A.	N.A.	62.1	24.6
Zr	95.31	74.72	77.89	82.77	83.8	61.55	N.A.	N.A.	N.A.	245	311
Nb	16.79	16.8	19.55	14.16	19.32	13.59	N.A.	N.A.	N.A.	69.7	33.5
Cs	9.9	5.65	13.78	8.1	13.91	9.78	N.A.	N.A.	N.A.	N.A.	N.A.
Ba	522.4	213.3	51.7	468.5	60.4	67.2	N.A.	N.A.	N.A.	238.0	244.0
La	32.89	22.37	23.05	27	21.87	18.89	N.A.	N.A.	N.A.	84.2	69
Ce	60.6	37.65	47.84	51.91	45.94	31.77	N.A.	N.A.	N.A.	166	128
Pr	6.23	3.93	5.14	5.72	5.8	4.58	N.A.	N.A.	N.A.	18.8	14.1
Nd	22.56	15.18	21.69	18.98	18.31	17.11	N.A.	N.A.	N.A.	52.2	47.9
Sm	4.8	1.75	7.02	3.66	5.6	3.4	N.A.	N.A.	N.A.	8.5	6.3
Eu	0.48	0.29	0.13	0.3	0.25	0.11	N.A.	N.A.	N.A.	0.6	0.78
Gd	4.43	2.25	4.76	3.75	6.84	2.89	N.A.	N.A.	N.A.	N.A.	4.51
Tb	0.67	0.35	0.73	0.7	0.82	1.1	N.A.	N.A.	N.A.	N.A	0.82
Dy	5.11	2.66	6.09	3.68	6.75	3.55	N.A.	N.A.	N.A.	4.2	3.67
Ho	0.98	0.38	1.1	0.97	1.48	0.67	N.A.	N.A.	N.A.	0.8	0.85
Er	2.81	1.36	4.69	2.24	4.29	3.12	N.A.	N.A.	N.A.	2.4	2.94
Tm	0.6	0.1	0.64	0.5	0.58	0.46	N.A.	N.A.	N.A.	0.5	0.43
Yb	4.62	1.43	5.57	3.45	6.93	4.01	N.A.	N.A.	N.A.	2.7	2.72
Lu	0.54	0.34	0.77	0.67	0.84	1.09	N.A.	N.A.	N.A.	0.4	0.4
Hf	3.32	3.76	3.37	3.42	3.14	1.55	N.A.	N.A.	N.A.	3.9	7.74
Ta	1.66	2.11	2.59	1.42	2.54	1.42	N.A.	N.A.	N.A.	2.3	1.95
Pb	34.76	33.36	38.82	31.68	37.99	28.61	N.A.	N.A.	N.A.	29.5	25.1
Th	32.19	15.87	39.08	27.29	41.54	29.16	N.A.	N.A.	N.A.	12.8	15.4
U	4.81	5.74	6.84	4.47	7.63	4.82	N.A.	N.A.	N.A.	4.1	3.5

Trace elements in p.p.m. by LA-ICP-MS.

Extended Data Table 3 | The posterior estimates of site for each archaeological sample in the major elements model

	Model Predicted Site					
Site	**Andes Pat**	**Antarctica**	**Maninjau**	**Rungwe**	**Toba**	**Turkana**
PP5-6	0.00	0.00	0.00	0.00	1.00	0.00
PP5-6	0.00	0.00	0.01	0.00	0.99	0.00
PP5-6	0.00	0.00	0.00	0.00	0.97	0.03
Vleesbaai	0.00	0.00	0.00	0.00	0.98	0.02
Vleesbaai	0.00	0.00	0.02	0.00	0.98	0.00
Vleesbaai	0.00	0.00	0.00	0.00	0.98	0.02
Vleesbaai	0.00	0.00	0.00	0.01	0.99	0.00
Vleesbaai	0.00	0.00	0.00	0.00	0.99	0.01
Vleesbaai	0.00	0.00	0.00	0.00	0.99	0.01
Vleesbaai	0.00	0.00	0.00	0.00	0.99	0.01

Values represent the proportion of MCMC iterations that assigned each of the six samples as belonging to each of the six sites.

Extended Data Table 4 | The posterior estimates of site for each archaeological sample in the trace elements model

Site	Model Predicted Site					
	Antarctica	Kenya	Maninjau	Rungwe	Toba	Turkana
PP5-6	0.00	0.00	0.00	0.00	0.99	0.01
PP5-6	0.00	0.01	0.00	0.00	0.99	0.00
Vleesbaai	0.00	0.00	0.00	0.00	1.00	0.00
Vleesbaai	0.00	0.00	0.00	0.00	1.00	0.00
Vleesbaai	0.00	0.00	0.00	0.00	1.00	0.00
Vleesbaai	0.00	0.01	0.00	0.01	0.97	0.01
Vleesbaai	0.00	0.00	0.00	0.00	1.00	0.00
Vleesbaai	0.00	0.00	0.00	0.00	1.00	0.00

Values represent the proportion of MCMC iterations that assigned each of the six samples as belonging to each of the six sites.

nature research

Corresponding author(s): Marean, Curtis W.

☐ Initial submission ☒ Revised version ☐ Final submission

Life Sciences Reporting Summary

Nature Research wishes to improve the reproducibility of the work that we publish. This form is intended for publication with all accepted life science papers and provides structure for consistency and transparency in reporting. Every life science submission will use this form; some list items might not apply to an individual manuscript, but all fields must be completed for clarity.

For further information on the points included in this form, see Reporting Life Sciences Research. For further information on Nature Research policies, including our data availability policy, see Authors & Referees and the Editorial Policy Checklist.

▶ Experimental design

1. **Sample size**

   Describe how sample size was determined.

   > Sample size was determined by the total sample that was excavated from the archaeological site.

2. **Data exclusions**

   Describe any data exclusions.

   > None

3. **Replication**

   Describe whether the experimental findings were reliably reproduced.

   > Since the geochemical analysis destroys the microscopic shard, no replication was possible.

4. **Randomization**

   Describe how samples/organisms/participants were allocated into experimental groups.

   > This is not relevant to our study.

5. **Blinding**

   Describe whether the investigators were blinded to group allocation during data collection and/or analysis.

   > This is not relevant to our study.

   Note: all studies involving animals and/or human research participants must disclose whether blinding and randomization were used.

6. **Statistical parameters**

   For all figures and tables that use statistical methods, confirm that the following items are present in relevant figure legends (or in the Methods section if additional space is needed).

n/a	Confirmed	
☐	☒	The exact sample size (n) for each experimental group/condition, given as a discrete number and unit of measurement (animals, litters, cultures, etc.)
☐	☒	A description of how samples were collected, noting whether measurements were taken from distinct samples or whether the same sample was measured repeatedly
☒	☐	A statement indicating how many times each experiment was replicated
☐	☒	The statistical test(s) used and whether they are one- or two-sided (note: only common tests should be described solely by name; more complex techniques should be described in the Methods section)
☐	☒	A description of any assumptions or corrections, such as an adjustment for multiple comparisons
☒	☐	The test results (e.g. P values) given as exact values whenever possible and with confidence intervals noted
☒	☐	A clear description of statistics including central tendency (e.g. median, mean) and variation (e.g. standard deviation, interquartile range)
☒	☐	Clearly defined error bars

   See the web collection on statistics for biologists for further resources and guidance.

▶ Software

7. Software

Describe the software used to analyze the data in this study.	OpenBUGS, a Bayesian simulation software. OxCal, a Bayesian age model software

For manuscripts utilizing custom algorithms or software that are central to the paper but not yet described in the published literature, software must be made available to editors and reviewers upon request. We strongly encourage code deposition in a community repository (e.g. GitHub). *Nature Methods* guidance for providing algorithms and software for publication provides further information on this topic.

▶ Materials and reagents

8. Materials availability

Indicate whether there are restrictions on availability of unique materials or if these materials are only available for distribution by a for-profit company.	No restrictions.

9. Antibodies

Describe the antibodies used and how they were validated for use in the system under study (i.e. assay and species).	This is not relevant to our study.

10. Eukaryotic cell lines

a. State the source of each eukaryotic cell line used.	This is not relevant to our study.
b. Describe the method of cell line authentication used.	This is not relevant to our study.
c. Report whether the cell lines were tested for mycoplasma contamination.	This is not relevant to our study.
d. If any of the cell lines used are listed in the database of commonly misidentified cell lines maintained by ICLAC, provide a scientific rationale for their use.	This is not relevant to our study.

▶ Animals and human research participants

11. Description of research animals

Provide details on animals and/or animal-derived materials used in the study.	This is not relevant to our study.

12. Description of human research participants

Describe the covariate-relevant population characteristics of the human research participants.	This is not relevant to our study.